

Reverse-time (and Kirchhoff) migration

Rodrigue Lelotte & Jules Sanchez

1. Preliminaries.

We consider the two-dimensional euclidian space as the medium, purported to be homogeneous ($c(x) \equiv 1$). Let us derive an analytical formula for the time-harmonic Green's function $\hat{G}_0(\omega, x, y)$, that is the Fourier transform of the Green's function $G_0(t, x, y)$ w.r.t. the time variable t , which we recall to satisfy the *Helmholtz equation*, i.e.

$$\Delta_x \hat{G}_0(\omega, x, y) + \omega^2 \hat{G}_0(\omega, x, y) = -\delta(x - y). \quad (1.1)$$

By taking the Fourier transform \mathcal{F}_x w.r.t. the space variable x of (1.1), we obtain

$$-|k|^2 \mathcal{F}_x \hat{G}_0(\omega, k, y) + \omega^2 \mathcal{F}_x \hat{G}_0(\omega, k, y) = -\exp(ik \cdot y)/(2\pi). \quad (1.2)$$

from which it follows that $\mathcal{F}_x \hat{G}_0(\omega, k, y) = -\exp(ik \cdot y)/(2\pi[\omega^2 - |k|^2])$. Therefore, one has

$$\hat{G}_0(\omega, x, y) = \mathcal{F}_x^{-1}[\mathcal{F}_x \hat{G}_0](\omega, x, y) = \frac{1}{(2\pi)^2} \int_{\mathbb{R}^2} \frac{\exp(ik \cdot (x - y))}{|k|^2 - \omega^2} dk. \quad (1.3)$$

Remark 1.1. Given a function $\mathbb{R} \ni r \mapsto f(r)$, one defines the ν -th Hankel transform of f as

$$\mathcal{H}_\nu[f](k) := \int_0^\infty f(r) J_\nu(kr) r dr,$$

where J_ν is the ν -th Bessel function of the first kind, that is

$$J_\nu(z) = \frac{(-i)^n}{2\pi} \int_0^{2\pi} \exp(iz \cos(\varphi) + in\varphi) d\varphi.$$

The ν -th Hankel transform expresses any given function f as a weighted-sum of an infinite number of rescaled Bessel functions of the first kind J_ν . That is, in comparison with the Fourier transform, the dual variable is no longer the frequency as it is some scaling factor.

Wisely rotating the frame of coordinates and carrying the computations into the polar domain yields that

$$\hat{G}_0(\omega, x, y) = \frac{1}{(2\pi)^2} \int_0^\infty \frac{r dr}{r^2 - \omega^2} \left[\int_0^{2\pi} \exp(ir \cos(\varphi)|x - y|) d\varphi \right] = \frac{1}{2\pi} \mathcal{H}_0 \left[\frac{1}{r^2 - \omega^2} \right] (|x - y|).$$

It remains to compute the 0-th Hankel transform of $f : r \mapsto 1/(r^2 - \omega^2)$. The neat trick here is to write

$$\mathcal{H}_0[f](k) = \int_0^\infty \mathcal{L}^{-1}[rf(r)](s) \mathcal{L}[J_0(kr)](s) ds,$$

where \mathcal{L} (resp. \mathcal{L}^{-1}) denotes the (resp. inverse) Laplace transform, and we have

$$\mathcal{L}[J_0(kr)](s) = \frac{1}{\sqrt{k^2 + s^2}}, \quad \mathcal{L}^{-1}[rf(r)] = \cos(-i\omega s),$$

so that we obtain (after change of variable $s \rightarrow s/|x - y|$)

$$\hat{G}_0(\omega, x, y) = \frac{1}{2\pi} \int_0^\infty \frac{\cos(-i|x - y|\omega s)}{\sqrt{s^2 + 1}} ds = \frac{1}{2\pi} K_0(-i|x - y|\omega) = \frac{i}{4} H_0(\omega|x - y|),$$

with K_0 the 0-th modified Bessel function of the second kind, and H_0 the 0-th Hankel function, where the last two equalities are common knowledge in the field of special functions. A more pedestrian derivation, not resorting to Hankel transform, is possible by using contour integrals.

2. Time-harmonic localization – full aperture.

2.1. Theoretical background

The embedded reflector x_{ref} is modeled by a local variation $V(x)$ of the propagation speed $c(x)$ in the vicinity of the reflector, where we suppose that $V(x) = \sigma_{\text{ref}} \cdot \mathbb{1}_{\Omega_{\text{ref}}}(x - x_{\text{ref}})$, where σ_{ref} is the target reflectivity and Ω_{ref} is the small scattering region of area ℓ_{ref}^2 which corresponds to the reflector apparatus. We assume that ℓ_{ref} is negligible w.r.t. the typical wavelength $\lambda = 2\pi/\omega$, such that we can suppose that $V(x) \simeq \sigma_{\text{ref}} \ell_{\text{ref}}^2 \cdot \delta(x - x_{\text{ref}})$. Using Born approximation, the Green's function reads

$$\hat{G}_{\text{ref}}(\omega, x, y) = \hat{G}_0(\omega, x, y) + \omega^2 \sigma_{\text{ref}} \ell_{\text{ref}}^2 \cdot \hat{G}_0(\omega, x, x_{\text{ref}}) \hat{G}_0(\omega, x_{\text{ref}}, y).$$

We record the impulse response matrix $(\hat{u}_{rs}(\omega))_{r,s}$, where $\hat{u}_{rs}(\omega)$ is the time-harmonic amplitude recorded by the r -th receiver when the s -th source emits a time-harmonic signal with unit amplitude and frequency ω . Equalizing the data, that is removing the incident field (*i.e.* not scattered), we have that

$$\hat{u}_{rs}(\omega) = \omega^2 \sigma_{\text{ref}} \ell_{\text{ref}}^2 \cdot \hat{G}_0(\omega, x_r, x_{\text{ref}}) \hat{G}_0(\omega, x_{\text{ref}}, x_s), \quad \forall r, s. \quad (2.1)$$

2.1.1. Reverse-time imaging

Recall that, in our context, the Reverse-time (RT) imaging function at the search point x^S is defined as

$$\mathcal{I}_{\text{RT}}(\omega, x^S) := \frac{1}{N^2} \sum_{r,s} \widehat{G}_0(\omega, x^S, x_r) \widehat{G}_0(\omega, x_s, x^S) \overline{\widehat{u}_{rs}(\omega)} \quad (2.2)$$

If the number of transducers is high enough, *i.e.* $N \gg 1$, we can assume that we have a continuum of transducers on $\partial B(0, R_0)$, so that plugging the impulse responses (2.1) into (2.2) yields the approximation (using *reciprocity* of the time-harmonic Green's function)

$$\mathcal{I}_{\text{RT}}(\omega, x^S) \simeq \omega^2 \sigma_{\text{ref}} \ell_{\text{ref}}^2 \cdot \left[\int_{x \in \partial B(0, R_0)} \widehat{G}_0(\omega, x^S, x) \overline{\widehat{G}_0(\omega, x_{\text{ref}}, x)} d\sigma(x) \right]^2.$$

Moreover, if $R_0 \gg 1$, we can invoke *Helmholtz-Kirchhoff identity*, so that we eventually have that the theoretical focal spot is given by

$$\mathcal{I}_{\text{RT}}(\omega, x^S) \simeq \sigma_{\text{ref}} \ell_{\text{ref}}^2 \cdot \Im \widehat{G}_0(\omega, x^S, x_{\text{ref}})^2 = \sigma_0 \cdot J_0^2(\omega |x^S - x_{\text{ref}}|)$$

with $\sigma_0 := \sigma_{\text{ref}} \ell_{\text{ref}}^2 / 16$.

2.1.2. Kirchhoff migration imaging

Let us now see how to extend the Kirchhoff migration (KM) imaging to the two-dimensional setting. For large $|z|$, we have the following simple asymptotic $H_0(z) \sim \sqrt{\frac{2}{\pi z}} \cdot e^{i(z - \pi/4)}$, so that if we neglect the variations of the amplitude term in the time-harmonic Green's function \widehat{G}_0 , one has

$$\mathcal{I}_{\text{RT}}(\omega, x^S) \simeq \frac{1}{N^2} \sum_{r,s} e^{i\omega(|x^S - x_r| - |x_{\text{ref}} - x_r|)} e^{i\omega(|x^S - x_s| - |x_{\text{ref}} - x_s|)} = \left[\frac{1}{N} \sum_r e^{i\omega(|x^S - x_r| - |x_{\text{ref}} - x_r|)} \right]^2.$$

Once again, if $N \gg 1$, we can assume that we have a continuum of transducers on $\partial B(0, R_0)$, so that

$$\mathcal{I}_{\text{RT}}(\omega, x^S) \simeq \left(\int_{x \in \partial B(0, R_0)} \exp \left[i\omega(|x^S - x| - |x_{\text{ref}} - x|) \right] d\sigma(x) \right)^2.$$

If $R_0 \gg \max\{|x^S|, |x_{\text{ref}}|\}$, we get from simple geometrical arguments that

$$|x^S - x| - |x_{\text{ref}} - x| \simeq \langle x_{\text{ref}} - x^S, R_0^{-1} x \rangle \quad \forall x \in \partial B(0, R_0).$$

Carrying the computations of the contour integral into the polar domain, that is writing $x = (R_0 \cos(\theta), R_0 \sin(\theta))$, and using the fact that there exists $\phi_{S,\text{ref}} \in [0, 2\pi)$ such that

$$\langle x_{\text{ref}} - x^S, R_0^{-1} x \rangle = |x^S - x_{\text{ref}}| \cos(\theta + \phi_{S,\text{ref}}), \quad \forall \theta \in [0, 2\pi),$$

we have

$$\int_{x \in \partial B(0, R_0)} \dots d\sigma(x) \simeq \int_0^{2\pi} \exp \left[i\omega |x^S - x_{\text{ref}}| \cos(\theta + \phi_{S,\text{ref}}) \right] d\theta,$$

so that we recognize the *0-th modified Bessel function I_0 of the first kind*, which we recall to have the integral representation $(2\pi)I_0(z) = \int_0^{2\pi} e^{z \cos(\theta)} d\theta$, therefore yielding we can take the *theoretical* Kirchhoff migration imaging function at the search point x^S to be

$$\mathcal{J}_{\text{KM}}^{(th)}(\omega, x^S) := I_0^2(i\omega |x^S - x_{\text{ref}}|).$$

In practice, we don't have access to x_{ref} , since we are precisely looking for this quantity. Therefore, a possible rough ansatz would be to simply define

$$\mathcal{J}_{\text{KM}}(\omega, x^S) := \frac{1}{N^2} \sum_{r,s} e^{i\omega(|x^S - x_s| + |x^S - x_r|)} \overline{\widehat{u}_{rs}(\omega)}.$$

2.2. Numerical experiments

Default parameters – We conduct a first numerical experiment with $N = 100$ transducers evenly-disposed on a circular array of radius $R_0 = 100$ centered at the origin. The reflector is positioned at locus $x_{\text{ref}} = (10, 20)$, and the source signals are taken to be time-harmonic waves of frequency $\omega = 2\pi$. The resolution of the discretization grid for the search space is taken to 20×20 centered at x_{ref} of underlying size 10×10 . Color-maps of the module of the time-reversal refocusing imaging functions obtained through RT and KM heuristics are displayed on fig. 1. We notice that KM and RT performances are very similar to one another, and that both techniques produce imaging functionals that are very close to the theoretical focal spot as derived above.

Moving the reflector – Getting the reflector closer to the boundary inherently deteriorates the resolution of the time-reverse refocusing. One possible way to overcome this problem is to increase the frequency ω of the search beam. Indeed, in the case where $\lambda \gg d(x_{\text{ref}}, \partial B(0, R_0))$ where $\lambda = 2\pi/\omega$, because the typical wavelength of the source beams is much larger than the distance between the near-located transducers and the reflector, we expect that those transducers that are close to x_{ref} will contaminate the overall refocusing process. This intuition is largely confirmed by our numerical experiment, see figs. 2 to 4. From those experiments, it pertains that KM imaging seems to perform slightly better than RT when the reflector is closed to the transducers array. This might be explained

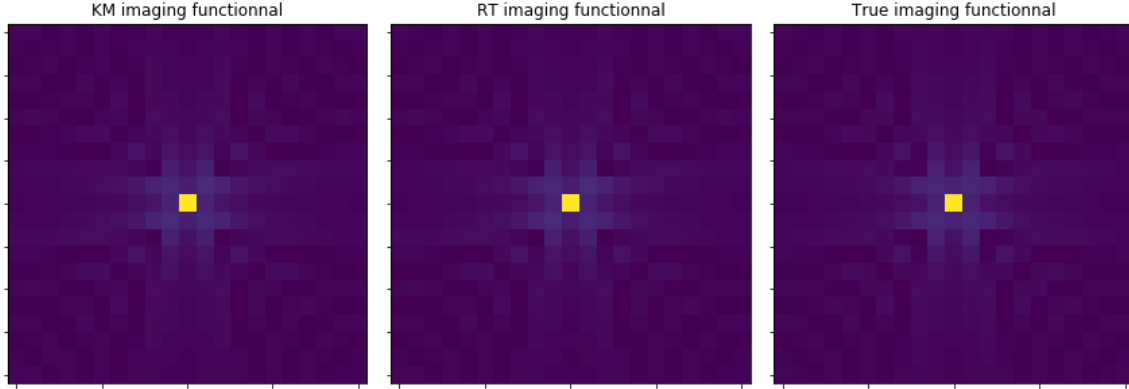


Fig. 1: Comparison of KM imaging (left) with RT imaging (center), and the theoretical focal spot (right). The search area is centered around $x_{\text{ref}} = (10, 20)$, with parameters $\omega = 2\pi$, $N = 100$ and $R_0 = 100$.

by the inherent singularities of the time-harmonic Green's function $\hat{G}_0(\omega, \cdot, \cdot)$ on its diagonal (*i.e.* $Y_0(x) \rightarrow -\infty$ as $x \rightarrow 0^+$). It is also important to notice that increasing the frequency translates into a higher demand for physical energy, which might come very costly.

Changing the number of transducers – Decreasing the number N of transducers also deteriorates the resolution, as confirmed by numerical experiments, see fig. 5 below. This is trivially fathomed: less transducers means that less information goes into the system, so that it is much harder to refocus in one pass. Note that this might be overcome by iterating the previous process several times, allowing for a better refocusing resolution at each pass.

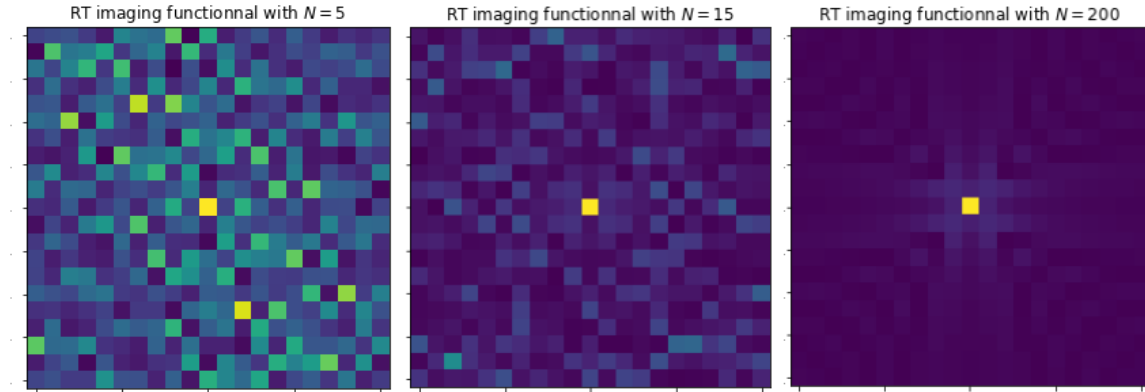


Fig. 5: Comparison of RT imaging with $N = 5$ transducers (left), $N = 15$ (center) and $N = 200$ (right). As expected, the resolution greatly deteriorates as N decreases. This applies to KM imaging as well.

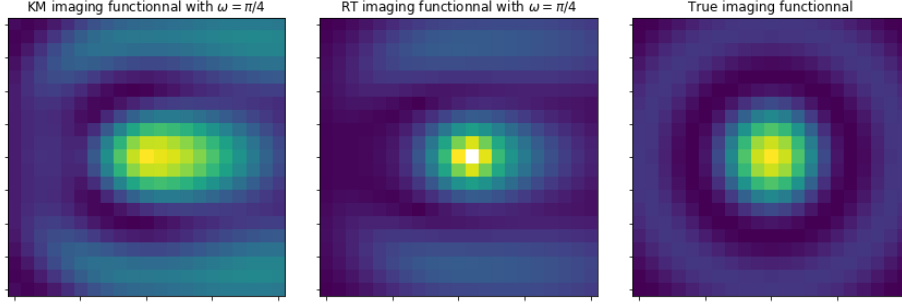


Fig. 2: Comparison of KM imaging (left) and RT imaging (center) with the theoretical spot (right) when the reflectors is positioned at locus $x_{\text{ref}} = (99.5, 0)$ and $\omega = \pi/4$ (all other parameters are left unchanged). White spot on the RT imaging corresponds to the closest transducer.

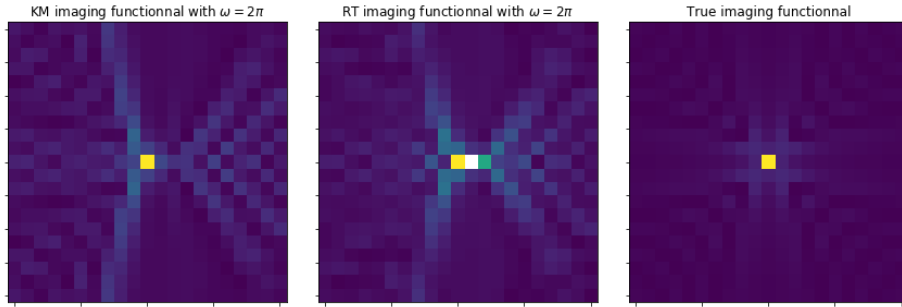


Fig. 3: Same comparison as above, but this time with the default frequency parameter $\omega = 2\pi$. Resolution is improved compared to the previous case, as expected from a physical point-of-view. Notice that KM performs slightly better than RT.

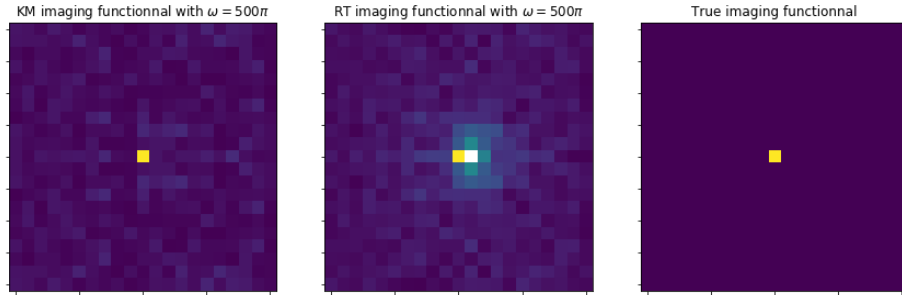


Fig. 4: Same comparison as above, but this time with very-high frequency $\omega = 500\pi$. Resolution is greatly improved in the search area compared to the previous cases, and we recover similar imaging functions as when the reflector was buried far away from the circular transducers array. Notice that KM performs with far more precision than RT.

3. Time-harmonic localization – partial aperture.

3.1. Theoretical background

3.1.1. A derivation for the cross-range focal spot

Let us give an *rough approximate* proof for the exact focal spot formula in the cross-range direction (x -direction) in the partial-aperture setting. First, we assume that we have a continuum of uniformly distributed transducers on $[-R_0/2, R_0/2]$. If the height L of the reflector x_{ref} (i.e. $x_{\text{ref}} = (0, L)$) is high enough, so that we can use Hankel's function expansion as before and neglect the variations of the amplitude term, we have the approximation

$$\mathcal{I}_{RT}(\omega, (x^S, 0)) \simeq \omega^2 \sigma_{\text{ref}} \ell_{\text{ref}}^2 \cdot \left[\int \mathbb{1}_{[-R_0/2, R_0/2]}(x_r) e^{i\omega(|x_{\text{ref}} - (x_r, 0)| - |x^S - x_r|)} dx_r \right]^2.$$

Under the regime where $L \gg R_0$, we have that

$$\begin{aligned} |x_{\text{ref}} - (x_r, 0)| - |x^S - x_r| &\simeq \left\langle (x^S, 0) - x_{\text{ref}}, \frac{(x_r, 0) - x_{\text{ref}}}{|(x_r, 0) - x_{\text{ref}}|} \right\rangle \\ &= |(x^S, 0) - x_{\text{ref}}| \cdot \underbrace{\text{Angle} \left((x^S, 0) - x_{\text{ref}}, (x_r, 0) - x_{\text{ref}} \right)}_{\simeq (x^S - x_r)/L}. \end{aligned}$$

Therefore, getting rid of the phase term, we obtain that

$$\begin{aligned} \mathcal{I}_{RT}(\omega, (x^S, 0)) &\simeq \omega^2 \sigma_{\text{ref}} \ell_{\text{ref}}^2 \cdot \left[\int \mathbb{1}_{[-R_0/2, R_0/2]}(x_r) e^{-i\omega x_r \frac{|(x^S, 0) - x_r|}{L}} dx_r \right]^2 \\ &= (2\pi)^2 \omega^2 \sigma_{\text{ref}} \ell_{\text{ref}}^2 \cdot \left[\hat{\mathbb{1}}_{[-R_0/2, R_0/2]} \left(\frac{|(x^S, 0) - x_r|}{L} \right) \right]^2, \end{aligned}$$

and using the well-known fact that $\hat{\mathbb{1}}_{[-R_0/2, R_0/2]}(\xi) = (\pi R_0/2) \cdot \text{sinc}(\xi R_0/2)$, we roughly find the mentioned result. Note that the oscillating behavior as $|x^S| \rightarrow \infty$ is coherent with the phenomenon of *edge diffraction*.

3.1.2. MUSIC-type imaging

Let us write $g(\omega, x^S)$ for the Green vector at the search point x^S , defined as the vector $g(\omega, x^S) := (\hat{G}_0(\omega, x^S, x_r))_r$. Then, it immediately follows from (2.1) that the impulse response matrix rewrites as $(\hat{u}_{rs}(\omega))_{r,s} \propto g(\omega, x_{\text{ref}}) g(\omega, x_{\text{ref}})^T$. Since the locus of x_{ref} is unknown, in practice, one can recover the Green vector $g(\omega, x_{\text{ref}})$ up to a multiplicative

constant by computing the first singular eigenvector v_1 of the impulse response matrix. From Courant-Fisher formula, one has

$$x_{\text{ref}} \in \arg \max_{x^S} \frac{g(\omega, x^S)^\dagger v_1 v_1^\dagger g(\omega, x^S)}{g(\omega, x^S)^\dagger g(\omega, x^S)}.$$

In the search space, we might neglect the denominator, and define the MUSIC-type imaging function to be

$$\mathcal{J}_{MU}(\omega, x^S) := |\langle \overline{v_1}, g(\omega, x^S) \rangle|^2,$$

in such a way that \mathcal{J}_{MU} is peaked at the reflector position x_{ref} .

Remark 3.1. *Note that, in the absence of measurement noise, since $v_1 \propto g(\omega, x_{\text{ref}})$, we have that*

$$\begin{aligned} |\mathcal{J}_{RT}(\omega, x^S)| &= |g(\omega, x^S)^T \overline{g(\omega, x_{\text{ref}})g(\omega, x_{\text{ref}})^T} g(\omega, x^S)| \\ &= |\langle \overline{g(\omega, x_{\text{ref}})}, g(\omega, x^S) \rangle|^2 \propto \mathcal{J}_{MU}(\omega, x^S) \end{aligned}$$

so that both functionals should theoretically yield the same results in absence of noise, as confirmed by numerical experiments (see below).

3.2. Numerical experiments

Default parameters – We conduct a first numerical experiment with $N = 100$ transducers evenly-disposed on the segment $[-R_0/2, R_0/2]$ of length $R_0 = 50$. The reflector is positioned on the z -axis at locus $x_{\text{ref}} = (0, 100)$. Once again, the resolution of the discretization grid for the search space is taken to 20×20 centered at x_{ref} of underlying size 10×10 . Color-maps obtained through RT, KM and the MUSIC heuristics are displayed on fig. 6. On fig. 7 we display the transverse and longitudinal resolutions. The performances of KT, KM and MUSIC in the transverse direction are very similar, and rather good compared to the theoretical baseline. On the longitudinal direction, RT and MUSIC display very similar results, as expected from the above remark, but are slightly off the fit with the theory compared to KM.

Playing with the aperture – A larger $R_0 \gg L$, (or equivalently a smaller L compared to R_0 in conjunction with a high enough search frequency ω) allows for a better refocusing. This is easily fathomed by intuition, as the limiting case $R_0 \rightarrow \infty$ essentially corresponds to a half-circle aperture, that is the bigger R_0 compared L , the more we surround the buried reflector and the more information is being retrieved about its location. A numerical experiment is conducted by selecting $R_0 = 1000$ (all the other parameters are left unchanged). The results are displayed on figs. 8 to 9. We see that the reflector is localized with great precision by every method, both in the x -direction and in the z -direction.

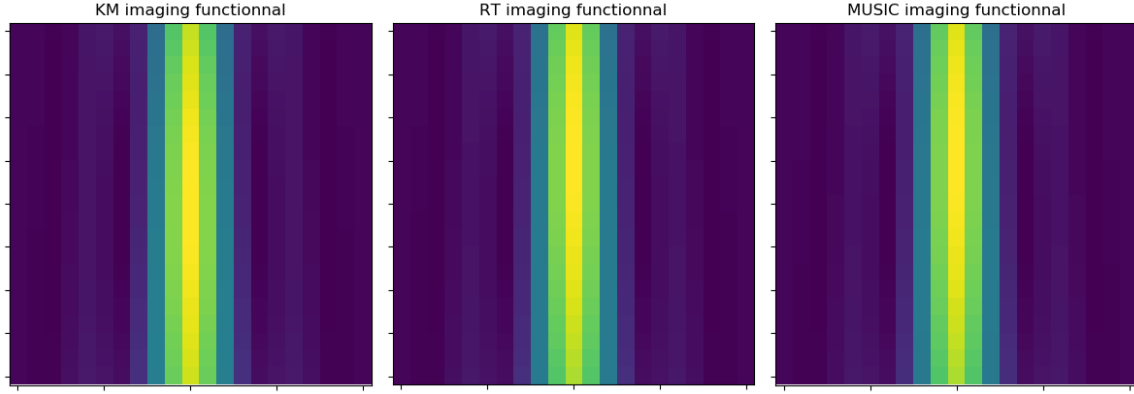


Fig. 6: Comparison of KM imaging (left) with RT imaging (center) and MUSIC-type imaging (right). We obtain very similar results.

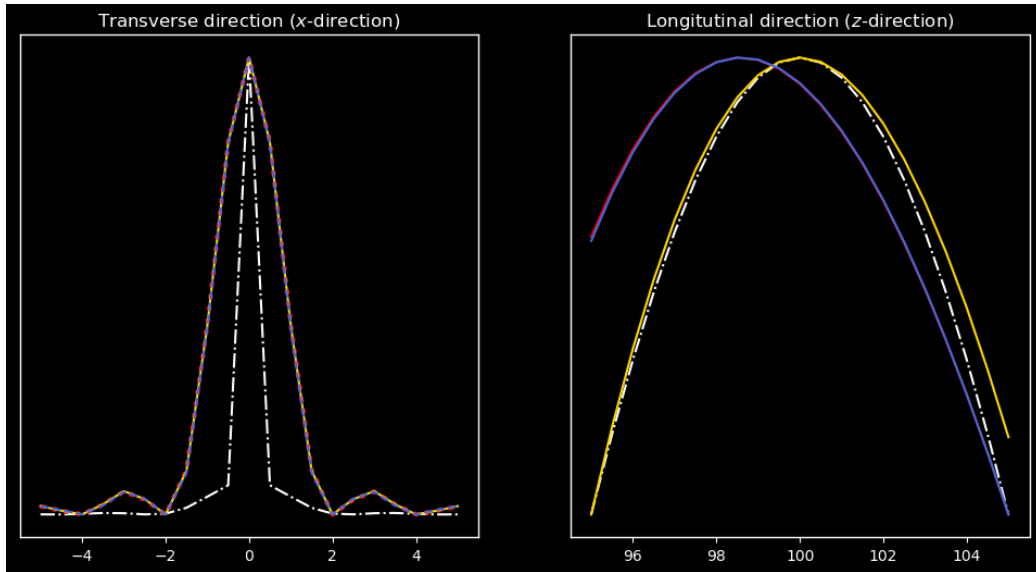


Fig. 7: Resolution in the transverse direction (*i.e.* x -direction) (left) and in the longitudinal direction (*i.e.* z -direction) (right). KM imaging is displayed in (gold), RT is in (red) and MUSIC is in (blue). The theoretical focal spots are given by the (white) dotted-lines. We have dotted and dashed the lines in the first graph to make every curves visible.

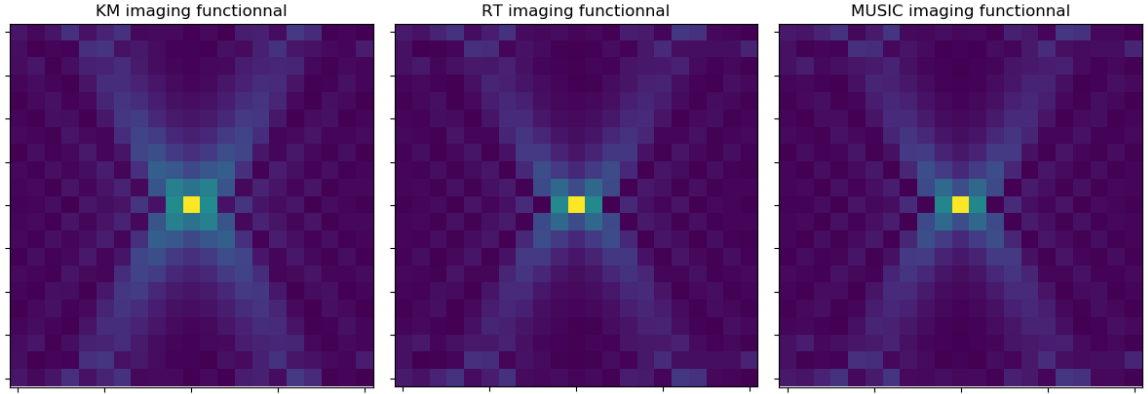


Fig. 8: Comparison of KM imaging (left) with RT imaging (center) and MUSIC-type imaging (right) in the case where $R_0 = 1000$. The refocusing for each method is very similar, and yields very good results.

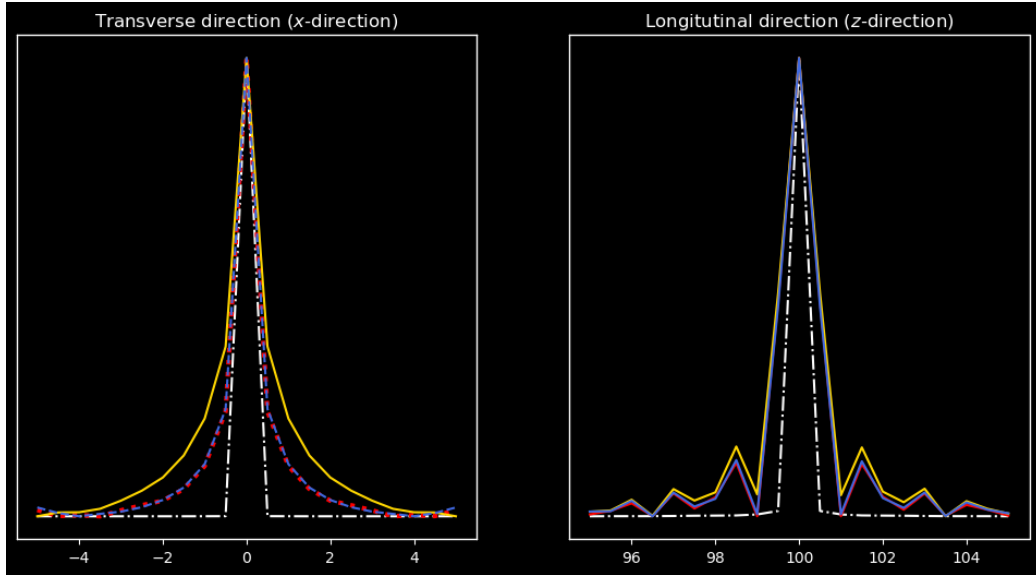


Fig. 9: Comparison of KM imaging (left) with RT imaging (center) and MUSIC-type imaging (right) in the case where $R_0 = 1000$. The transverse and longitudinal resolutions are very good.

4. Time-dependent localization – partial aperture.

We now assume that the sources emit a broadband signal f with $\hat{f}(\omega) = \mathbb{1}_{[\omega_0-B, \omega_0+B]}(\omega)$. In this context, the Reverse-time imaging function at the search point x^S reads

$$\mathcal{I}_{RT}(\omega_0, B, x^S) = \frac{1}{N^2} \int_{\omega_0-B}^{\omega_0+B} \sum_{r,s} \hat{G}_0(\omega, x^S, x_r) \hat{G}_0(\omega, x_s, x^S) \overline{\hat{u}_{rs}(\omega)} d\omega$$

and the Kirchhoff-migration imaging function reads

$$\mathcal{I}_{KM}(\omega_0, B, x^S) := \frac{1}{N^2} \int_{\omega_0-B}^{\omega_0+B} \sum_{r,s} e^{i\omega(|x^S-x_s|+|x^S-x_r|)} \overline{\hat{u}_{rs}(\omega)} d\omega.$$

We might wonder about the effect of using a broadband signal rather than a time-harmonic signal as before. Using the theoretical formulae for the focal spots in the transverse and longitudinal direction, we see that the transverse width of the peak at the reflector is $\lambda_0|x_{\text{ref}}|/R_0$ with $\lambda_0 = 2\pi/\omega_0$ the wavelength of the central frequency ω_0 (*i.e.* this is the so-called *Rayleigh resolution formula*), and we notice that it doesn't depend on the bandwidth B , while the longitudinal width of the peak, *i.e.* $\pi/2B$, does. Therefore, a bigger bandwidth $B \gg 1$ allows for a better longitudinal resolution in the search domain. The limiting case $B \rightarrow 0$ corresponds to the time-harmonic signal (in the distributional sense).

4.1. Numerical experiments

Default parameters – We conduct a first numerical experiment with $N = 40$ transducers evenly-disposed on the segment $[-R_0/2, R_0/2]$ of length $R_0 = 20$. The reflector is positioned on the z -axis at locus $x_{\text{ref}} = (0, 100)$. The central frequency is $\omega_0 = 2\pi$ and the bandwidth is selected at $B = 0.05\omega_0$. The integral $\int_{\omega_0-B}^{\omega_0+B} \dots$ is computed by sampling over 20 frequencies. Color-maps obtained through RT and KM are displayed on fig. 10. On fig. 11 we display the transverse and longitudinal resolutions. The performances of KT and KM are both similar in the transverse and the longitudinal direction, and rather good compared to the theoretical baselines.

Playing with the bandwidth – Let us decrease B to $0.0001\omega_0$ (and take $R_0 = 100$). As expected, we obtain something similar to the previous section, see fig. 12 and fig. 13. Also, as expected, increasing B enhances the resolution in the longitudinal direction (see notebook).

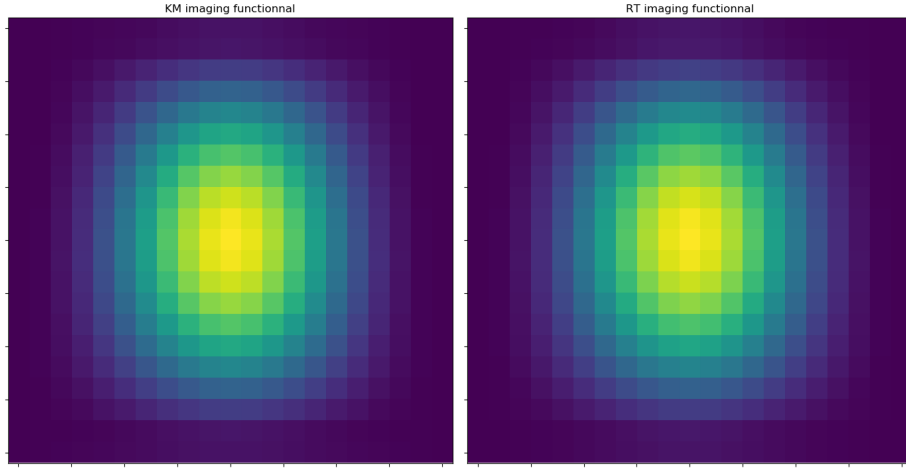


Fig. 10: Comparison of KM imaging (left) and RT imaging (center) with a broadband signal of central frequency $\omega_0 = 2\pi$ and bandwidth $B = 0.05\omega_0$, with $N = 40$ and $R_0 = 20$. We obtain very similar results for KM and RT.

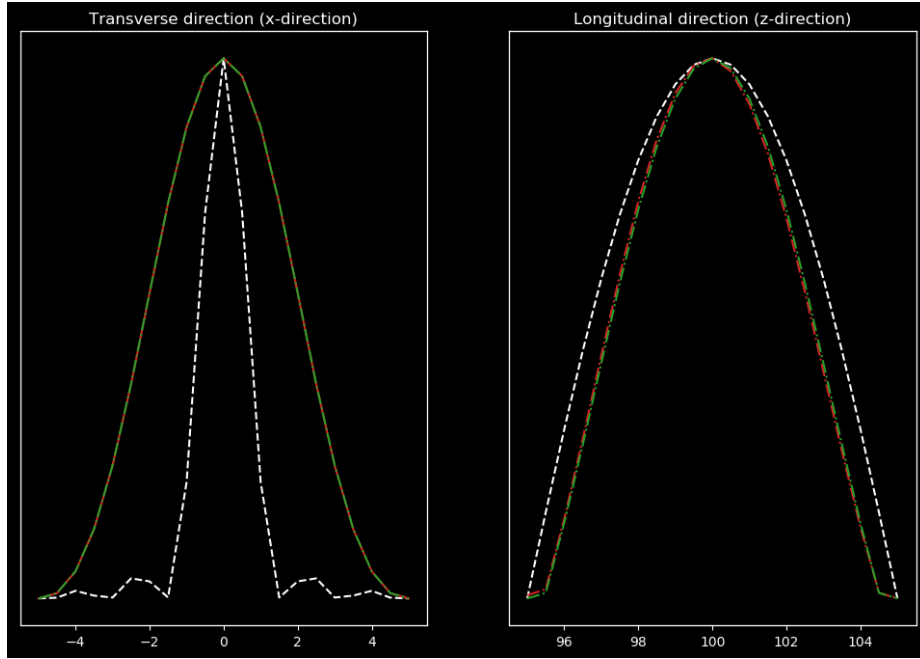


Fig. 11: Resolution in the transverse direction (*i.e.* x -direction) (left) and in the longitudinal direction (*i.e.* z -direction) (right) with default parameters. RT imaging is in (red) and KM is in (green). The theoretical focal spots are given by the white dotted-lines.

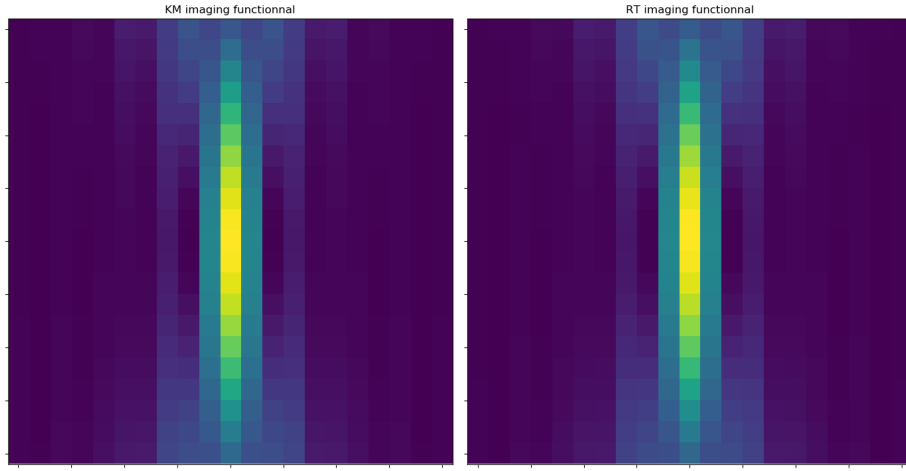


Fig. 12: Comparison of KM imaging (left) and RT imaging (center) with a broadband signal of size $B = 0.0001\omega_0$ with $R_0 = 100$. The results are similar to that of the previous section, see fig. 6

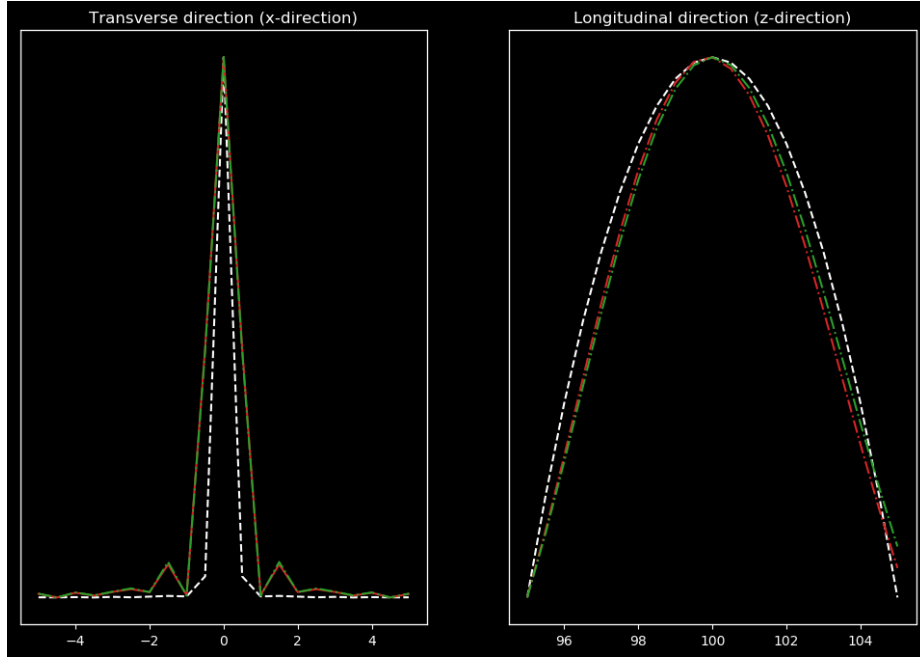


Fig. 13: Resolution in the transverse direction (*i.e.* x -direction) (left) and in the longitudinal direction (*i.e.* z -direction) (right) with $B = 0.0001\omega_0$ and $R_0 = 100$. RT imaging is in (red) and KM is in (green). The theoretical focal spots are given by the white dotted-lines.

5. Stability with respect to measurement noise.

5.1. Theoretical background

We add measurement noises to our previous settings, that is, we consider that the recorded signals are of the form $\hat{u}_{rs}(\omega) + W_{rs}^{(1)}(\omega) + iW_{rs}^{(2)}(\omega)$, where $W_{rs}^{(1)}(\omega)$ and $W_{rs}^{(2)}(\omega)$ are i.i.d. Gaussian random variables with mean zero and variance $\sigma^2/2$. Let us write $\mathcal{J}_0(\omega, x^S)$ for the unperturbed imaging function (2.2), such that the Reverse-time imaging function at the search point x^S reads $\mathcal{J}_{RT}(\omega, x^S) = \mathcal{J}_0(\omega, x^S) + \mathcal{J}_{\text{noise}}(\omega, x^S)$, where

$$\mathcal{J}_{\text{noise}}(\omega, x^S) := \frac{1}{N^2} \sum_{r,s} \hat{G}_0(\omega, x^S, x_r) \hat{G}_0(\omega, x_s, x^S) [W_{rs}^{(1)}(\omega) - iW_{rs}^{(2)}(\omega)].$$

Under those hypotheses, the imaging function $\mathcal{J}_{RT}(\omega, x^S)$ defines a complex Gaussian random field of mean $\mu(x^S) = \mathcal{J}_0(\omega, x^S)$ whose relation function is zero, *i.e.*

$$\mathbb{E}[(\mathcal{J}_{RT}(\omega, x^S) - \mathcal{J}_0(\omega, x^S))(\mathcal{J}_{RT}(\omega, x^{S'}) - \mathcal{J}_0(\omega, x^{S'}))] = 0, \quad \forall x^S, x^{S'}$$

and whose covariance is given by

$$\begin{aligned} C_\omega(x^S, x^{S'}) &= \mathbb{E}[(\mathcal{J}_{RT}(\omega, x^S) - \mathcal{J}_0(\omega, x^S)) \overline{(\mathcal{J}_{RT}(\omega, x^{S'}) - \mathcal{J}_0(\omega, x^{S'}))}] \\ &= \frac{\sigma^2}{N^2} \left[\frac{1}{N} \sum_r \hat{G}_0(\omega, x^S, x_r) \overline{\hat{G}_0(\omega, x^{S'}, x_r)} \right]^2 \end{aligned}$$

5.1.1. Localization error in the full-aperture setting

In the full-aperture setting, the theoretical covariance function is given by

$$C_\omega(x^S, x^{S'}) = \sigma_{\text{noise}}^2 \tilde{C}_\omega(x^S - x^{S'})$$

with

$$\tilde{C}_\omega(x) := J_0^2(\omega|x|), \quad \sigma_{\text{noise}}^2 := \frac{\sigma^2 \sigma_{\text{ref}}^2 \ell_{\text{ref}}^2}{16N^2}.$$

The signal-to-noise ratio is therefore given by $\text{SNR} = N/\sigma$. Let us compute the hotspot matrix $\Lambda = -\text{Hess}[\tilde{C}_\omega](0)$. Using that $J'_0 = -J_1$, we have

$$-\nabla_x J_0^2(\omega|x|) = 2\omega J_0(\omega|x|) J_1(\omega|x|) \cdot \frac{x}{|x|},$$

and therefore

$$\begin{aligned} -\frac{1}{2\omega} \text{Hess}[\tilde{C}_\omega](x) &= J_0(\omega|x|) J_1(\omega|x|) \cdot \nabla_x \left(\frac{x}{|x|} \right) + \frac{x}{|x|} \nabla_x (J_0(\omega|x|) J_1(\omega|x|))^T \\ &= J_0(\omega|x|) J_1(\omega|x|) \left(\frac{I_2}{|x|} - \frac{xx^T}{|x|^3} \right) + \omega \left(\frac{1}{2} J_0(\omega|x|) (J_0(\omega|x|) - J_2(\omega|x|)) - J_1^2(\omega|x|) \right) \cdot \frac{xx^T}{|x|^2}, \end{aligned}$$

and using the fact that $J_0(0) = 1$, $J_2(0) = 0$ and $J_1(x) = \frac{x}{2} - \frac{x^3}{16} + \mathcal{O}(x^4)$, we obtain that $\Lambda = \omega^2 I_2$. Therefore, the quantity $\hat{x} := \arg \max_{x^S} |\mathcal{J}_{RT}(\omega, x^S)|$ is an unbiased (to the leading order in $1/\text{SNR}$) estimator of x_{ref} , and its covariance is given by

$$\mathbb{E}[(\hat{x} - x_{\text{ref}})(\hat{x} - x_{\text{ref}})^T] = \frac{1}{2\text{SNR}^2} \cdot \Lambda^{-1} = \frac{\sigma^2}{2\omega^2 N^2} \cdot I_2,$$

which in particular means that the localization errors are independent along the x and the z axis. Therefore, we shall be expected that the mean and the standard deviation of the localization error will decrease as $1/N$.

5.1.2. Transverse localization error in the partial-aperture setting

Let us give a *very rough* derivation for the localization error in the transverse direction in the case of the partial-aperture setting with time-harmonic signal. Supposing that $-\frac{R_0}{2} \leq x^S \leq x^{S'} \leq \frac{R_0}{2}$, and using Hankel's function expansion as before, we have the theoretical equality as $N \rightarrow \infty$

$$\begin{aligned} C_\omega((x^S, 0), (x^{S'}, 0)) &= \frac{\sigma^2}{N^2} \left[\int_{[-R_0/2, R_0/2]} e^{i\omega(|x^S - x_r| - |x^{S'} - x_r|)} dx_r \right]^2 \\ &= \frac{\sigma^2}{N^2} \left[e^{i\omega(x^S - x^{S'})} \left(x^S + \frac{R_0}{2} \right) + e^{i\omega(x^{S'} - x^S)} \left(\frac{R_0}{2} - x^{S'} \right) + \omega^{-1} \mathcal{O}_{\sim 0}(|x^S - x^{S'}|) \right]^2. \end{aligned}$$

Supposing that $\omega \gg |x^S - x^{S'}|$ and that $R_0 \gg \max\{|x^S|, |x^{S'}|\}$, we can roughly approximate the preceding quantity as

$$C_\omega((x^S, 0), (x^{S'}, 0)) \simeq \frac{\sigma^2}{N^2} \cdot R_0^2 \cos^2(\omega(x^S - x^{S'})),$$

which rewrites as $C_w((x^S, 0), (x^{S'}, 0)) = \sigma_{\text{noise}}^2 C_\omega(x^S - x^{S'})$ with

$$\sigma_{\text{noise}}^2 = \sigma^2 R_0^2 / N^2, \quad \text{and} \quad \tilde{C}_\omega(x) = \cos^2(\omega x).$$

The signal-to-noise ratio is therefore given by $\text{SNR} = N/\sigma$, and the hotspot volume is given by $-\tilde{C}'_\omega(0) = 2\omega^2$. Therefore, the localization error has (to the leading order $1/\text{SNR}$) mean 0 and variance $\sigma^2/(4\omega^2 N^2)$. Hence, we shall be expected that the mean and the standard deviation of the localization error will decrease as $1/N$.

5.2. Numerical experiments

For each previous configuration, we run the different imaging functions with two levels of noise, that is $\sigma = 0.2$ and $\sigma = 1$. For $\sigma = 0.2$, each algorithm still displays very decent result, but with $\sigma = 1$, the performances greatly deteriorates. On figs. 14 to 15, we display the color-maps for KM and RT imaging in the full-aperture setting. On figs. 16 to 19, we display the results of RT, KM and MUSIC in the partial-aperture setting with time-harmonic signal. On figs. 20 to 23, we display the results of RT and KM in the partial-aperture setting with a broadband signal.

Remark 5.1. *We were quite disappointed with the overall results of MUSIC in presence of measurement noise. Indeed, we were expecting that it would reveal itself to be more performant than KM and RT in this setting, because only considering the first singular vector of the impulse response matrix should theoretically extract a great deal of the signal from the noisy environment, compared to KM and RT that blindly consider the entire signal without any kind of denoising procedure. That being said, MUSIC is far less demanding from a computational perspective compared to RT and KM, which counters for the overall bad performance.*

Finally, we went off to compute the mean and the standard deviation of the localization error w.r.t. different parameters (namely N , R_0 and B). All the plots are available in the notebook. Sadly enough, we obtained results that were rather bizarre (*i.e.* no particular trends), except in the case of the full-aperture setting w.r.t. the number of transducers N . In this case (see figs. 24 to 25), we observe that for $\sigma = 0.01$, the mean and the standard deviation of the localization error is 0. This is explained by the fact that the measurement noise is too small to disturb the refocusing. For higher levels of noise, *i.e.* $\sigma = 0.5$ and $\sigma = 1$, we see that as N increases from 1 to 20, the mean of the localization decreases (which is confirmed by the theory as derived above). Nevertheless, the standard deviation doesn't seem to be affected by N , though it should according the formula derived above.

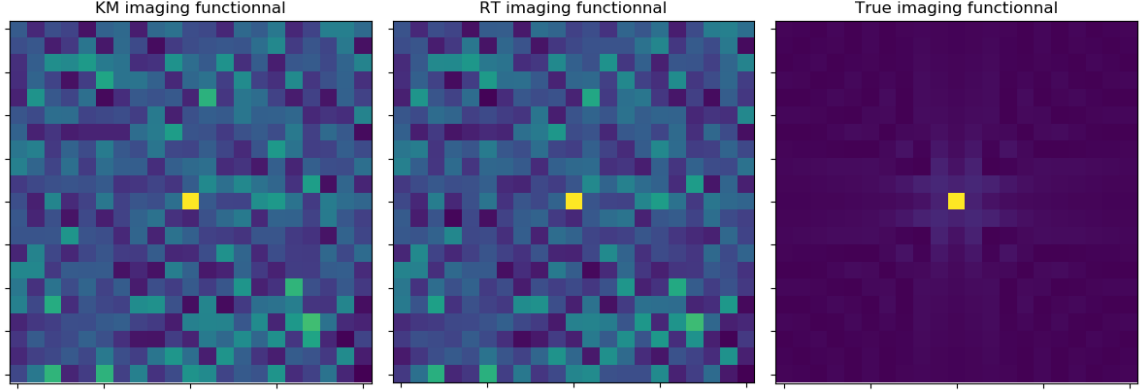


Fig. 14: Comparison of KM imaging (left) and RT imaging (center) with $\sigma = 0.2$ (and the default parameters) in the full-aperture setting. The refocusing is still rather good compared to the theoretical baseline.

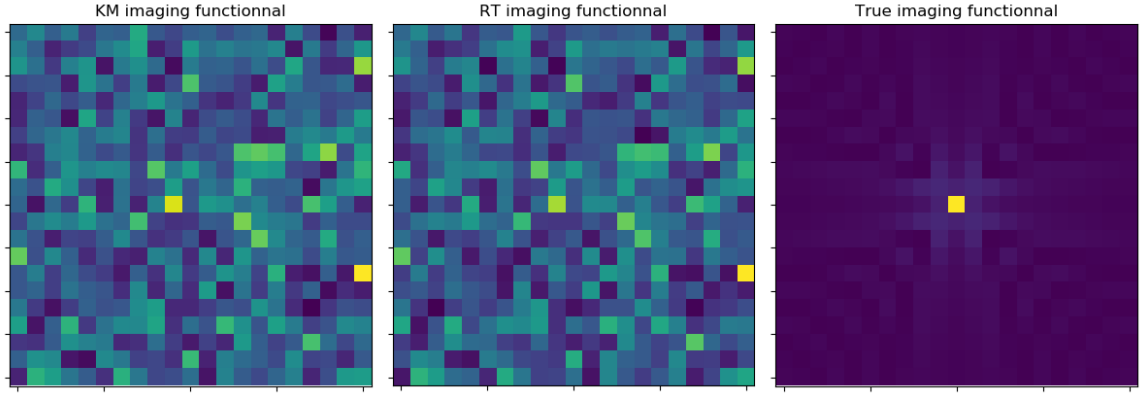


Fig. 15: Comparison of KM imaging (left) and RT imaging (center) with $\sigma = 1$ (and the default parameters) in the full-aperture setting. The refocusing is greatly deteriorated compared to $\sigma = 0.2$. IN fact, the signal is almost drawn in the measurement noise.

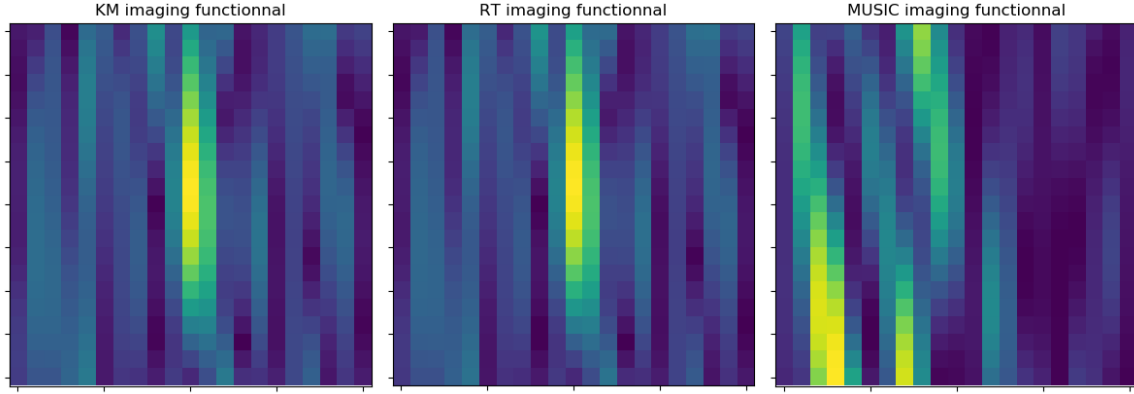


Fig. 16: Comparison of KM imaging (left), RT imaging (center) and MUSIC (right) with $\sigma = 0.2$ (and the default parameters) in the partial-aperture setting with time-harmonic signal. KM and RT are still performing well, but MUSIC is off the fit in the transverse direction (see fig. 17 below)

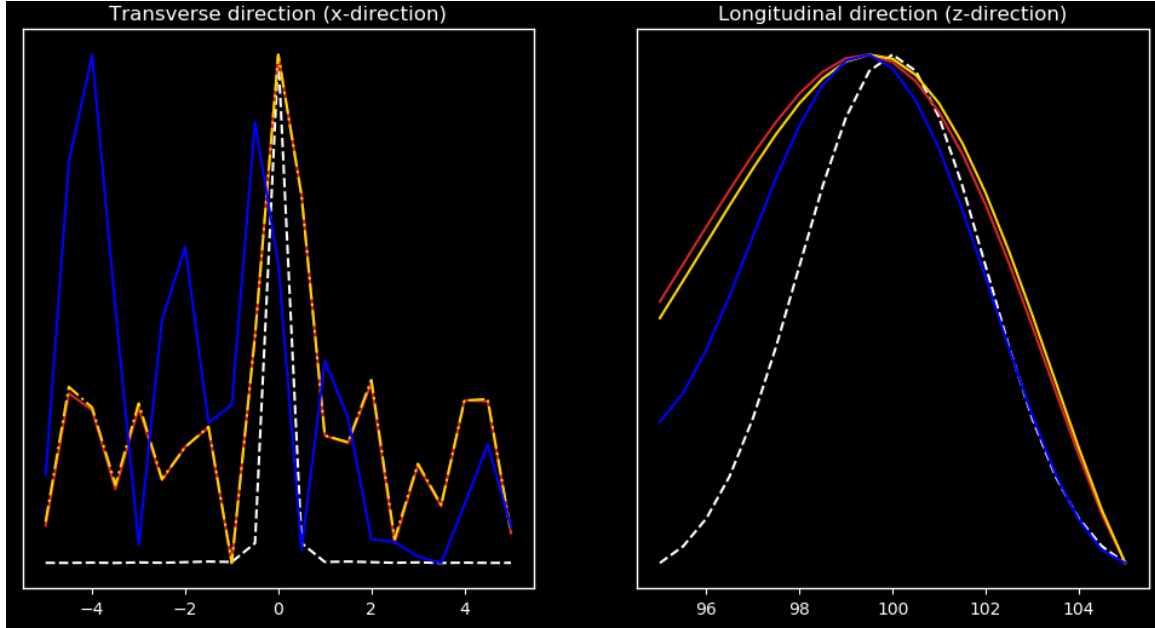


Fig. 17: Resolution in the transverse direction (*i.e.* x -direction) (left) and in the longitudinal direction (*i.e.* z -direction) (right) with $\sigma = 0.2$ for the partial-aperture setting with time-harmonic signal. KM imaging is displayed in (gold), RT is in (red) and MUSIC is in (blue).

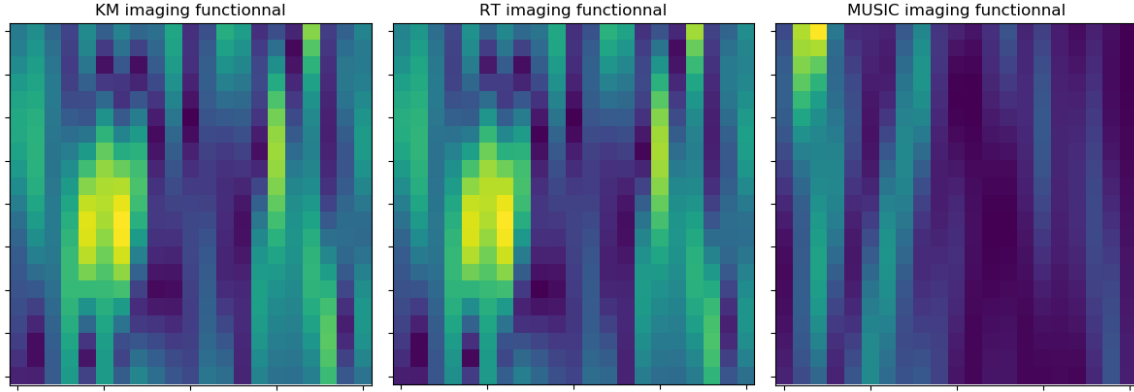


Fig. 18: Comparison of KM imaging (left), RT imaging (center) and MUSIC (right) with $\sigma = 1$ (and the default parameters) in the partial-aperture setting with time-harmonic signal. The refocusing is greatly deteriorated compared to $\sigma = 0.2$, both in the transverse and longitudinal directions (see fig. 19 below).

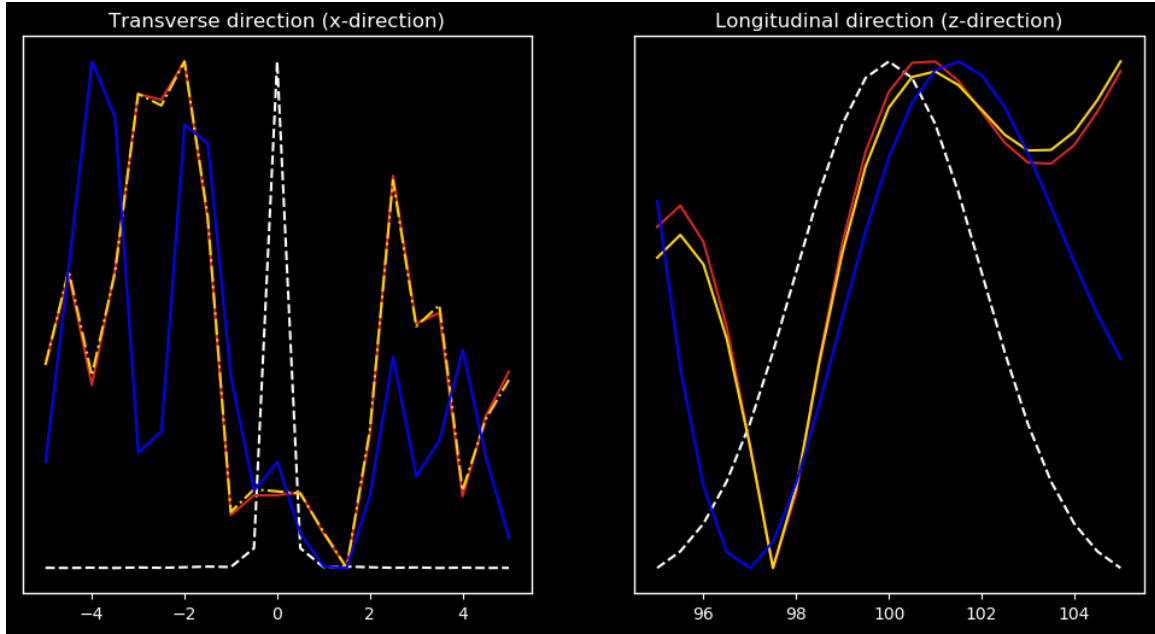


Fig. 19: Resolution in the transverse direction (*i.e.* x -direction) (left) and in the longitudinal direction (*i.e.* z -direction) (right) with $\sigma = 1$ for the partial-aperture setting with time-harmonic signal. KM imaging is displayed in (gold), RT is in (red) and MUSIC is in (blue).

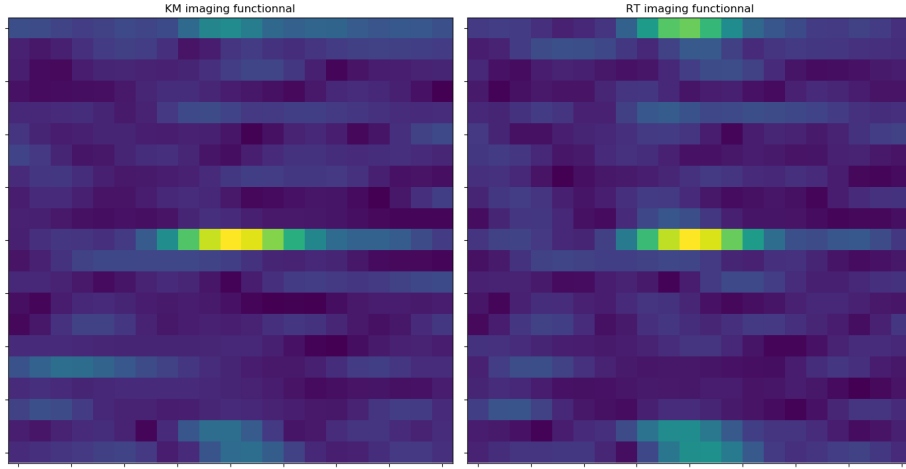


Fig. 20: Comparison of KM imaging (left) and RT imaging (right) with $\sigma = 0.2$ (and the default parameters) in the partial-aperture setting with broadband signal. We observe rather good performances.

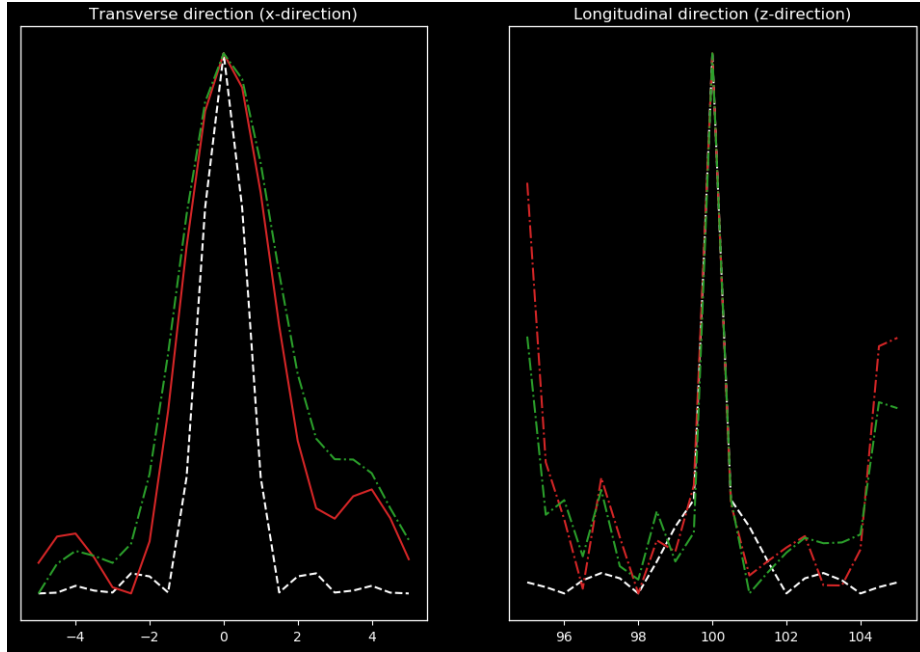


Fig. 21: Resolution in the transverse direction (*i.e.* x -direction) (left) and in the longitudinal direction (*i.e.* z -direction) (right) with $\sigma = 0.2$ for the partial-aperture setting with broadband signal. RT imaging is in (red) and KM is in (green).

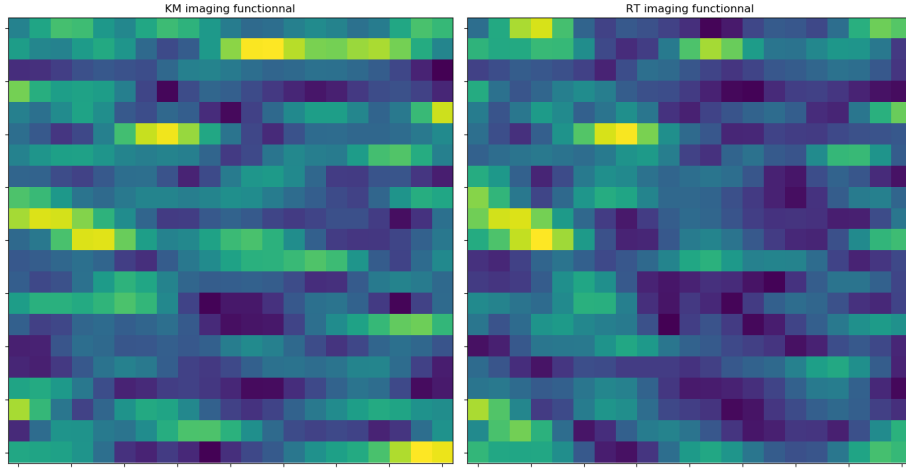


Fig. 22: Comparison of KM imaging (left) and RT imaging (right) with $\sigma = 0.1$ (and the default parameters) in the partial-aperture setting with broadband signal. The refocusing is greatly deteriorated compared to $\sigma = 0.2$ (see fig. 23 below).

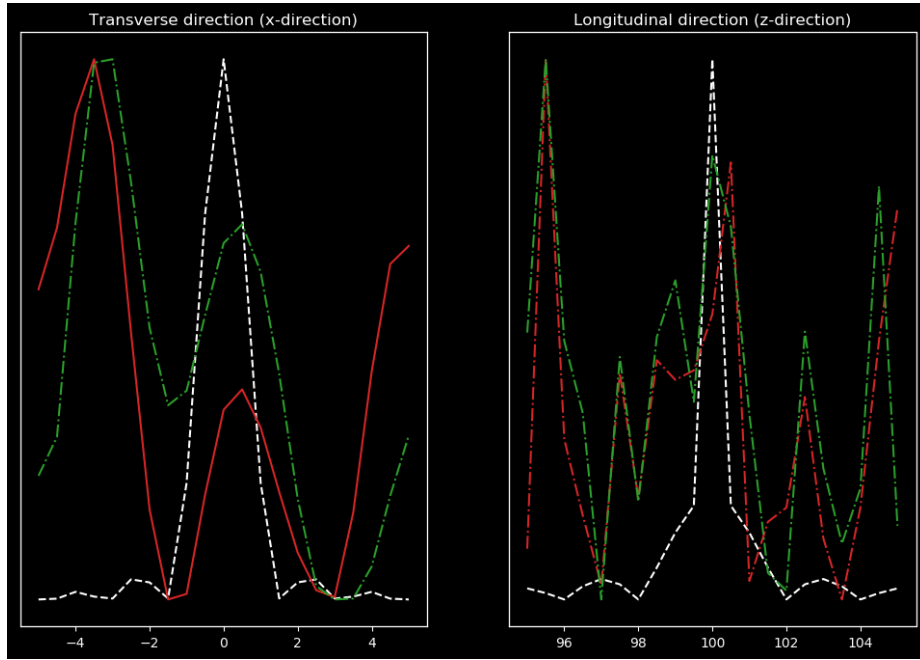


Fig. 23: Resolution in the transverse direction (*i.e.* x -direction) (left) and in the longitudinal direction (*i.e.* z -direction) (right) with $\sigma = 1$ for the partial-aperture setting with broadband signal. RT imaging is in (red) and KM is in (green).

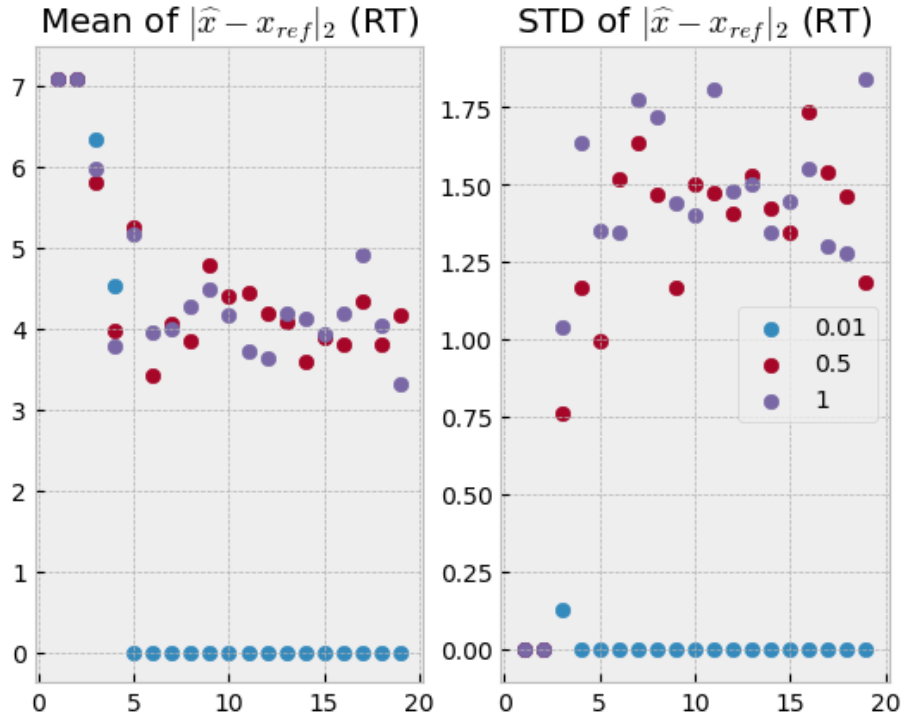


Fig. 24: The mean (left) and standard deviation (right) of the localization error in the RT imaging w.r.t. to N . Each point was estimated from a sample of size 30. .

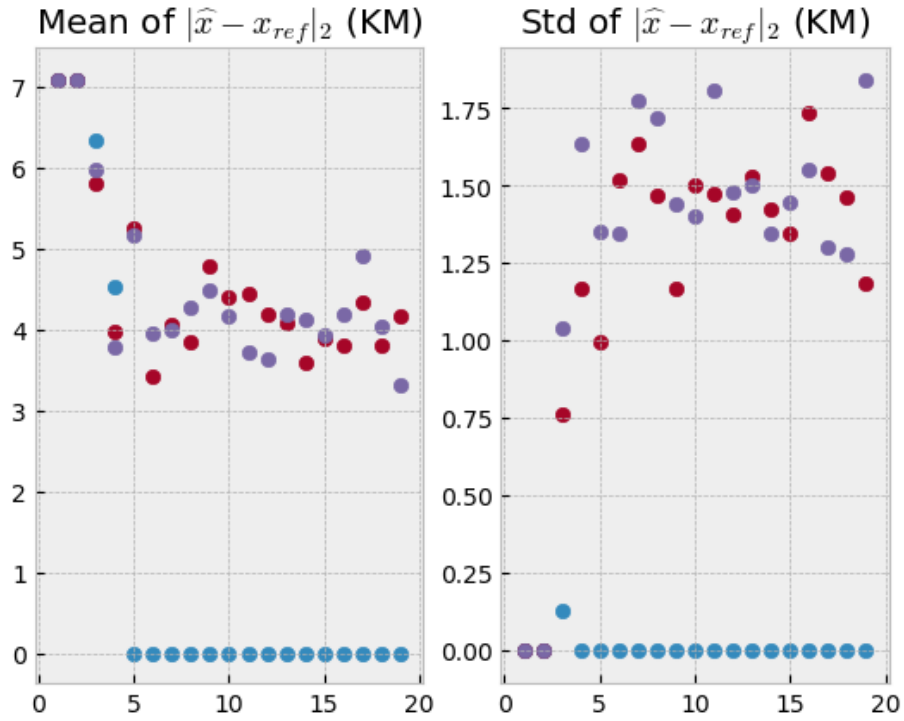


Fig. 25: Same as above, but in the case of KM imaging